

Direct visualization of bottlebrush polymer conformations in the solid state

Jonathan M. Chan, Avram C. Kordon, Ruimeng Zhang, and Muzhou Wang

Department of Chemical and Biological Engineering, Northwestern University, Evanston, Illinois 60208, United States

Supporting Information

Table of Contents

1. Confirmation of macroinitiator chemical structure by NMR	2
2. Determination of dye concentration on bottlebrush polymer by UV-Vis	4
3. Characterization of bottlebrush polymer molecular weight by GPC	6
4. Calculation of expected average contour length of bottlebrush.....	7
5. Additional super-resolution images of bottlebrush polymers.....	8
6. Calculation of impurity concentration	9
7. Selecting bottlebrush features for analysis	9
8. Images of control conditions.....	9
9. Details for simulating super-resolution bottlebrush images	12
10. Comment on bottlebrush width and side chain length.....	14
11. Monte Carlo simulation exploring effect of confinement on persistence length.....	15

1. Confirmation of macroinitiator chemical structure by NMR

The structures of PBIEM-based macroinitiators were verified using ^1H NMR in CDCl_3 . This NMR spectrum was compared to the spectrum of the starting polymer, PHEMA, as provided by Polymer Source.

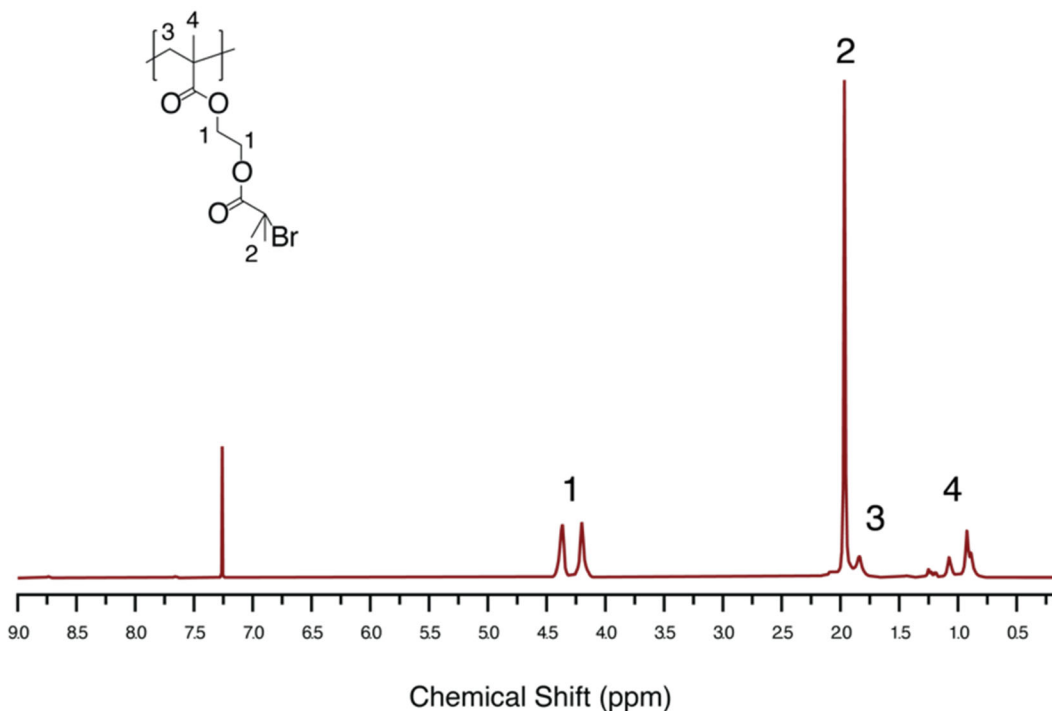


Figure S1: NMR spectrum of PBIEM macroinitiator.

^1H NMR (500 MHz, CDCl_3) **1** (s, $\delta = 4.20, 4.37$, 4H), **2** (s, $\delta = 1.97$, 6H), **3** (s, $\delta = 1.84$, 2H), **4** ($\delta = 0.89-1.23$, 3H)

For the random copolymer macroinitiators synthesized, ^1H NMR was used to determine the number of bromide-containing repeat units, which act as initiation sites for atom transfer radical polymerization to grow. Comparing Figures S2 and S3 to Figure S1, we confirm a distinction between the fully bromide-functionalized macroinitiator with the partially functionalized bromide species. We compared peaks 3 and 4 in the spectra of the copolymer macroinitiator (Figure S2-3) to determine the fraction of bromide-containing repeat units along the chain.

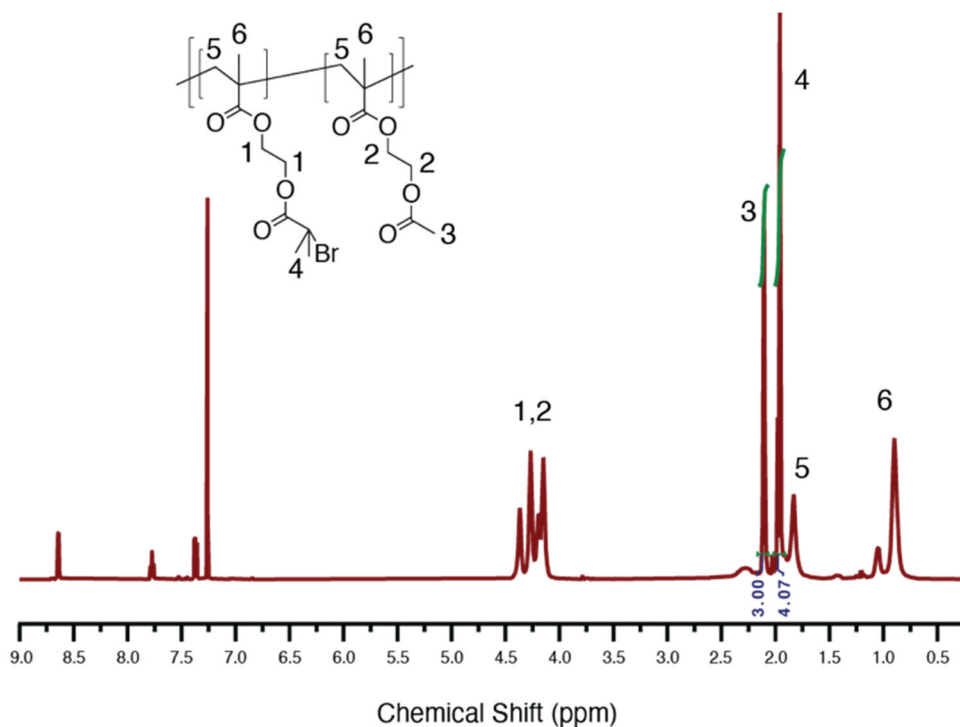


Figure S2: NMR spectrum of 40% bromide-functionalized PBIEM macroinitiator.

^1H NMR (500 MHz, CDCl_3) **1,2** ($\delta = 4.37, 4.27, 4.20, 4.15, 8\text{H}$), **3** (s, $\delta = 2.11, 6\text{H}$), **4** (s, $\delta = 1.96, 3\text{H}$), **5** (s, $\delta = 1.83, 4\text{H}$), **6** ($\delta = 0.93\text{-}1.53, 6\text{H}$).

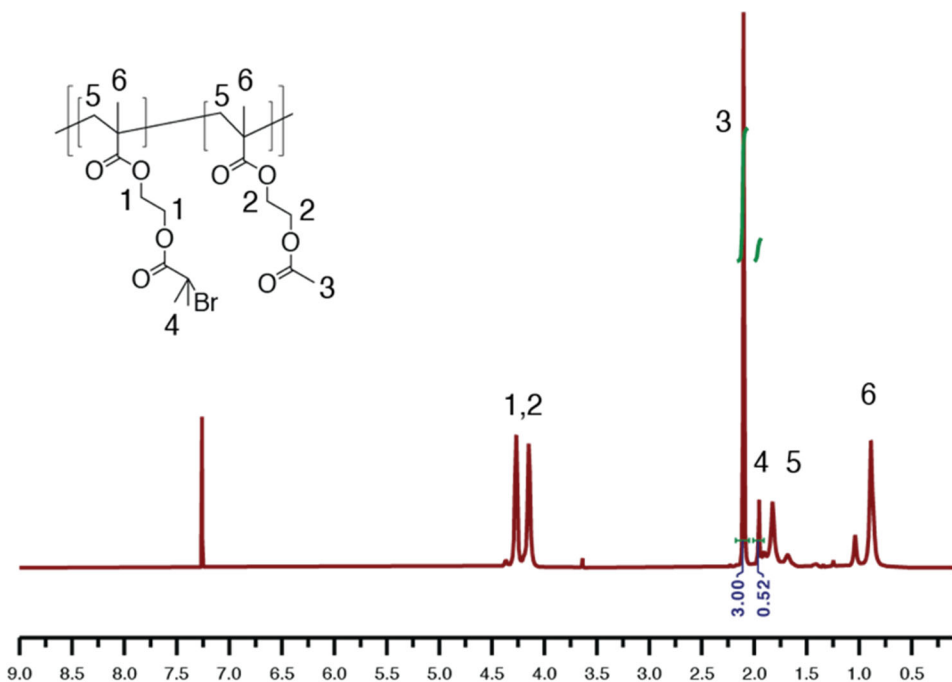


Figure S3: NMR spectrum of 8% bromide-functionalized PBIEM macroinitiator.

^1H NMR (500 MHz, CDCl_3) **1,2** ($\delta = 4.37, 4.27, 4.20, 4.15, 8\text{H}$), **3** (s, $\delta = 2.11, 6\text{H}$), **4** (s, $\delta = 1.96, 3\text{H}$), **5** (s, $\delta = 1.83, 4\text{H}$), **6** ($\delta = 0.93\text{-}1.53, 6\text{H}$).

2. Determination of dye concentration on bottlebrush polymer by UV-Vis

While the ratio between dye to monomer was chosen to be 0.25-0.5 wt% for synthesis, we determined the concentration of dye on the final bottlebrush polymers using UV-Vis spectroscopy.

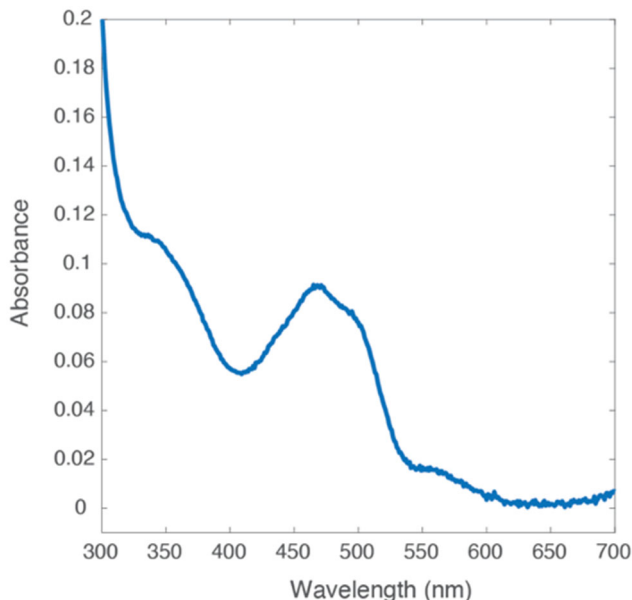


Figure S4: UV-Vis spectra of one dyed bottlebrush polymer (Sample 3 from Table 1 in the main body). During synthesis, 0.25% dye by weight of total monomer was added to the reaction, resulting in a bottlebrush that contains 0.23% dye by weight of total polymer.

The absorbance of the dyed bottlebrush from UV-Vis spectroscopy can be used to determine the concentration of dye using Beer's Law,

$$A = \epsilon b C,$$

where A is the absorbance, ϵ is the extinction coefficient, b is the path length, and C is the concentration. This calculation was performed at the isosbestic point at 395 nm, because at this wavelength the absorbance is not affected by the ratio between activated and deactivated dyes. The extinction coefficient was determined measuring the absorbances of samples with varying dye concentrations, and the value ϵ was found from the slope of the linear relationship. A sample calculation of dye concentration is provided below for a UV-Vis measurement of the bottlebrush sample with $M_{sc} = 2,030$ g/mol and $z = 1$ (Sample 3 from Table 1 in the main body) with a concentration of 1 mg/mL in THF:

$$C_{dye} = \frac{M_{dye} A}{\epsilon b} = \frac{(0.0188)(824.85 \text{ g/mol})}{(6658 \text{ M}^{-1}\text{cm}^{-1})(1 \text{ cm})} = 0.0023 \text{ mg/mL}$$

$$\frac{C_{dye}}{C_{bottlebrush}} = \frac{0.0023 \text{ mg/mL}}{1.0 \text{ mg/mL}} \times 100\% = 0.23\%$$

M_{dye} is the molecular weight of the dye, C_{dye} is the concentration of dye, and $C_{bottlebrush}$ is the concentration of the bottlebrush polymer. From the absorbance as the isosbestic point at 395 nm with $\epsilon = 6658 \text{ M}^{-1}\text{cm}^{-1}$, we calculate a dye concentration of 0.23% by weight, which is in good agreement with the targeted dye concentration of 0.25% by weight from synthesis conditions. We expect similar results for all dyed bottlebrush polymers synthesized through this study.

In order to confirm covalent attachment of dye onto the bottlebrush polymer, we analyzed the dyed polymers using a GPC equipped with a UV-Vis detector (Fig. S5). The RI and UV-Vis peaks of the dyed polymer match directly, confirming attachment.

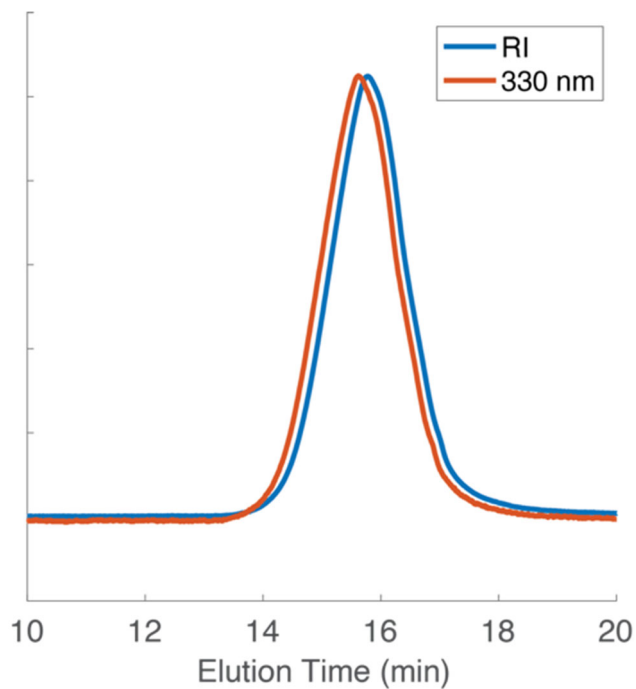


Figure S5: GPC trace of dyed bottlebrush sample from refractive index and UV-Vis at 330 nm, the peak absorbance wavelength for the deactivated form of the dye. The peak from the UV-Vis signal appearing simultaneously with the peak from the RI peak confirms dye attachment on the bottlebrush polymer.

3. Characterization of bottlebrush polymer molecular weight by GPC

To verify the synthesis of bottlebrush polymers, we compared the bottlebrush polymer to the macroinitiator using GPC (Fig. S6). Here, we show one trace for a PMMA bottlebrush sample plotted along with the PBIEM macroinitiator. Because the bottlebrush polymer elutes distinctly earlier than the macroinitiator, we are confident that the grafting-from polymerization to form the side chains was successful.

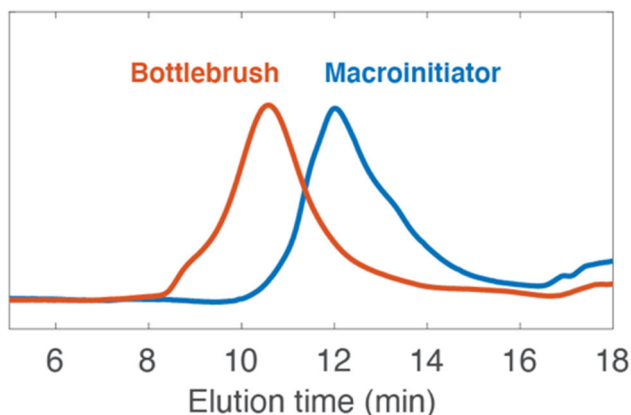


Figure S6: GPC trace of PBIEM macroinitiator ($M_n = 598.9$ kg/mol, $D = 1.18$) and sample of PMMA bottlebrush polymer ($M_{sc} = 3,500$ g/mol, $z = 1$, Sample 5 from Table 1 in the main body)

In order to characterize the side chain molecular weight of the bottlebrush polymers, we analyzed the cleaved side chains (see Experimental Section) using MALS-GPC to directly determine their molecular weight.

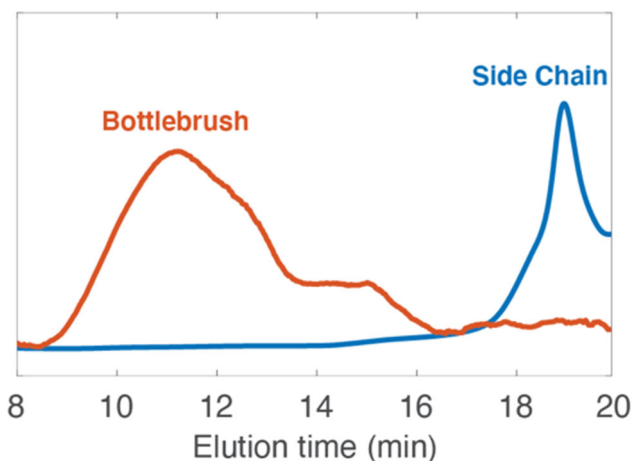


Figure S7: GPC trace of a PMMA bottlebrush polymer ($M_{sc} = 5,800$ g/mol, $z = 0.4$, Sample 9 from Table 1 in the main body).

Figure S7 shows the GPC traces of a PMMA bottlebrush polymer with its corresponding cleaved side chain. Based on the molecular weight of the full bottlebrush polymer, the side chains are expected to have a $M_n = 5.32$ kg/mol. The molecular weight of the side chain is determined to be $M_n = 5.80$ kg/mol, which is within 10% of the estimated value. This is consistent with all cleaved side chain samples. These results provide assurance that the grafting density is close to the fraction of bromide-containing repeat units along the macroinitiators, and therefore can be

treated the same. The agreement between the estimated and measured results of the side chain molecular weight do not reflect phenomena such as termination by combination, which would result in coupling bottlebrush polymers together or cause side chains along the same bottlebrush to loop. These effects are not expected to have a major impact on the conformation of the backbone in our studies.

4. Calculation of expected average contour length of bottlebrush

Based on a C-C bond length of 0.154 nm and an angle of 109.5° based on tetrahedral geometry, we estimate each methacrylate-based repeat unit to have a length of 0.25 nm. Based on a DP_n of 1870 for poly(hydroxyethyl methacrylate) (Polymer Source), we calculate an average polymer length of 460 nm for a fully extended backbone. Because we only expect a fully extended conformation for bottlebrushes with a densely grafted backbone, we may expect the contour lengths of some bottlebrushes in super-resolution images to be shorter than this prediction. Because of this as well as the dispersity of the backbone molecular weight, we judiciously accept features above 200 nm in length.

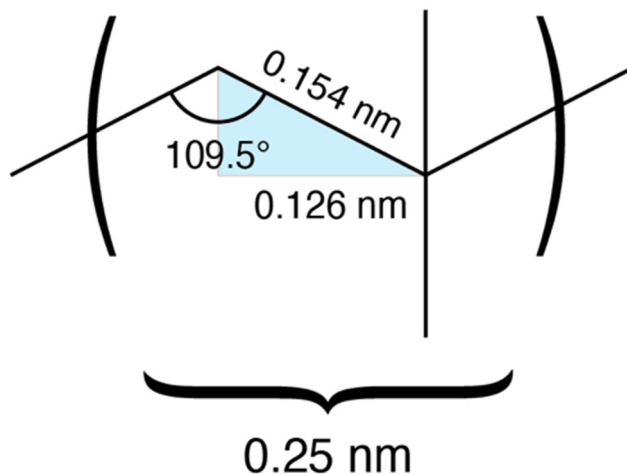


Figure S8: Determination of expected length of methacrylate-based repeat unit. This calculation was used to determine the expected average length of bottlebrush polymers in super-resolution images.

5. Additional super-resolution images of bottlebrush polymers

Fluorescent foreign species have a potential to appear as artifacts in the final image. These features tend to be small and have negligible effects on the bottlebrush images used for analysis. The sample super-resolution image shown in Figure 3 has had artifacts removed to visualize the bottlebrush features more clearly. A version of that image without artifacts removed is shown in Figure S9.

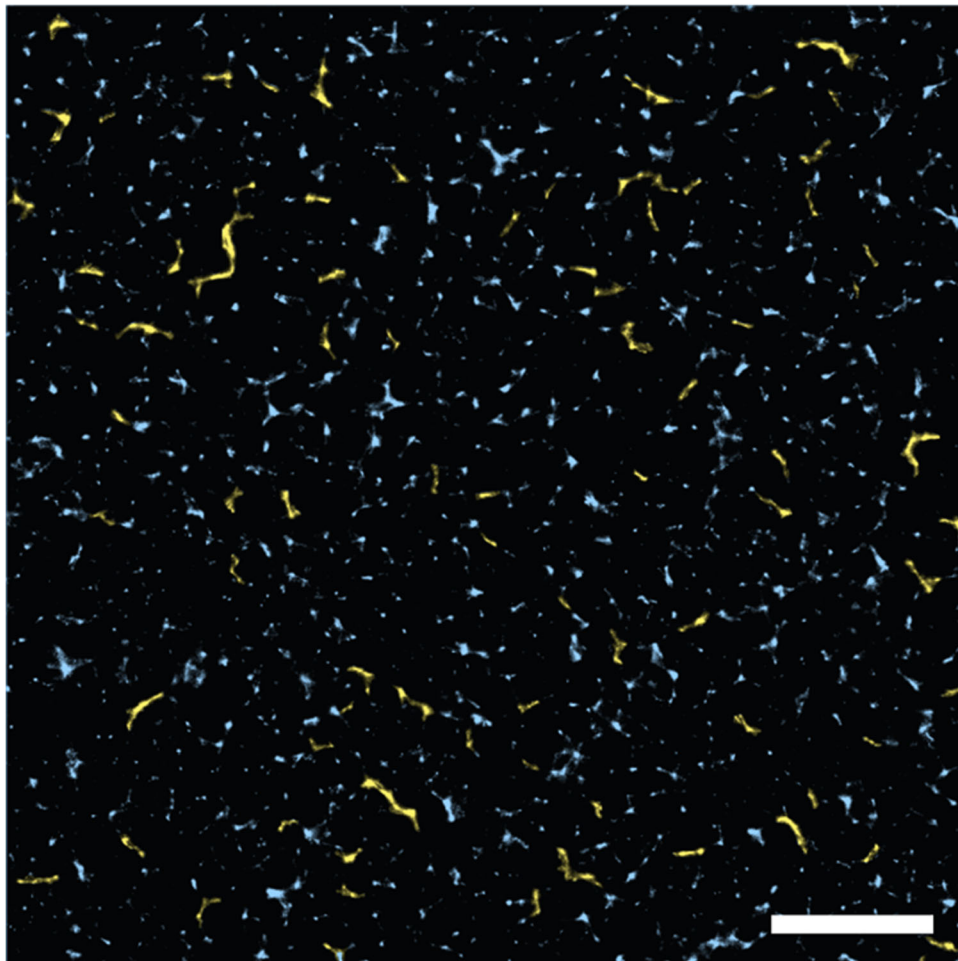


Figure S9: Dual-toned super-resolution image of bottlebrushes in linear matrix. Features chosen for analysis have been recolored in yellow, and the remaining features have been recolored in blue. A number of small features are visible due to background fluorescence and contamination. These features do not affect analysis and have no major impact on the relevant elongated features of interest. Scale bar is 2 μm .

Additional super-resolution images of bottlebrush polymers with different conditions are shown in Figure S10. We observe variations in the rigidity of bottlebrush features between these three conditions. While deviations in rigidity are difficult to see between some samples, these images were chosen to illustrate the variations in conformations of bottlebrushes within samples.

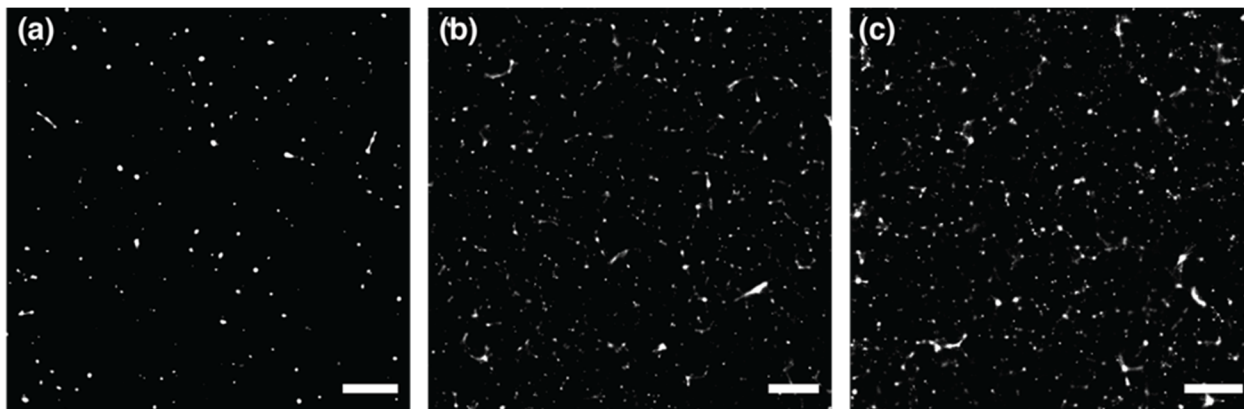


Figure S10: Sample super-resolution images of different bottlebrush conditions. (a) $M_{sc} = 3,500$, $z = 1$, 1:0.03 linear PMMA to dyed PMMA bottlebrush (b) $M_{sc} = 3,300$, $z = 0.4$ 1:0.06 linear PMMA to dyed PMMA bottlebrush (c) $M_{sc} = 3,120$, $z = 0.08$ 1:0.06 linear PMMA to dyed PMMA bottlebrush. Scale bar is 2 μm .

6. Calculation of impurity concentration

Based on Figure S11, which shows approximately ten features per 1 μm^2 area in a 40 nm thick film, and based on the assumption that each feature correlates to a single impurity molecule of mass 1000 amu, we calculate the concentration of impurity molecules within the system as,

$$\left(\frac{10 \text{ molecules}}{(1 \mu\text{m})^2 (0.040 \mu\text{m})} \right) \left(\frac{1000 \text{ amu}}{1 \text{ molecule}} \right) \left(\frac{(10^4 \mu\text{m})^3}{1 \text{ cm}^3} \right) \left(\frac{1 \text{ cm}^3}{1.18 \text{ g}} \right) \left(\frac{1.66 \times 10^{-24} \text{ g}}{1 \text{ amu}} \right) = 4.15 \times 10^{-7}$$

$$= 0.415 \text{ ppm}$$

7. Selecting bottlebrush features for analysis

Features were first filtered by size, selecting only objects possessing Feret diameters larger than 200 nm for analysis. After choosing these features, each were manually sorted through and selected for further analysis. The chosen features fulfill three requirements:

1. Features must have a thin, elongated shape with a consistent width
2. Features cannot be too large
3. Features should be easily analyzed by skeletonization

For the first criterion, not only is the shape of the feature important, but also a consistent width differentiates a feature from a series of serendipitously positioned artifacts. Additionally, while features are already filtered by a minimum size, features that are very large are not selected for analysis as they are not expected to be a single bottlebrush but rather overlapping chains. Finally, the skeletonized trace must accurately fit the feature and be devoid of branching in order for features to be selected.

8. Images of control conditions

To confidently proceed in our super-resolution imaging, we prepared a number of control conditions to see whether the elongated features that appear in the dyed bottlebrush samples

appear in samples that do not contain dyed bottlebrush. Here, we imaged a linear PMMA film that contains no dye, a linear PMMA film that contains dye physically mixed into the polymer solution prior to spin-coating, and a linear PMMA film that contains dyed linear PMMA. None of these cases produced images with elongated features similar to those in the dyed bottlebrush samples.

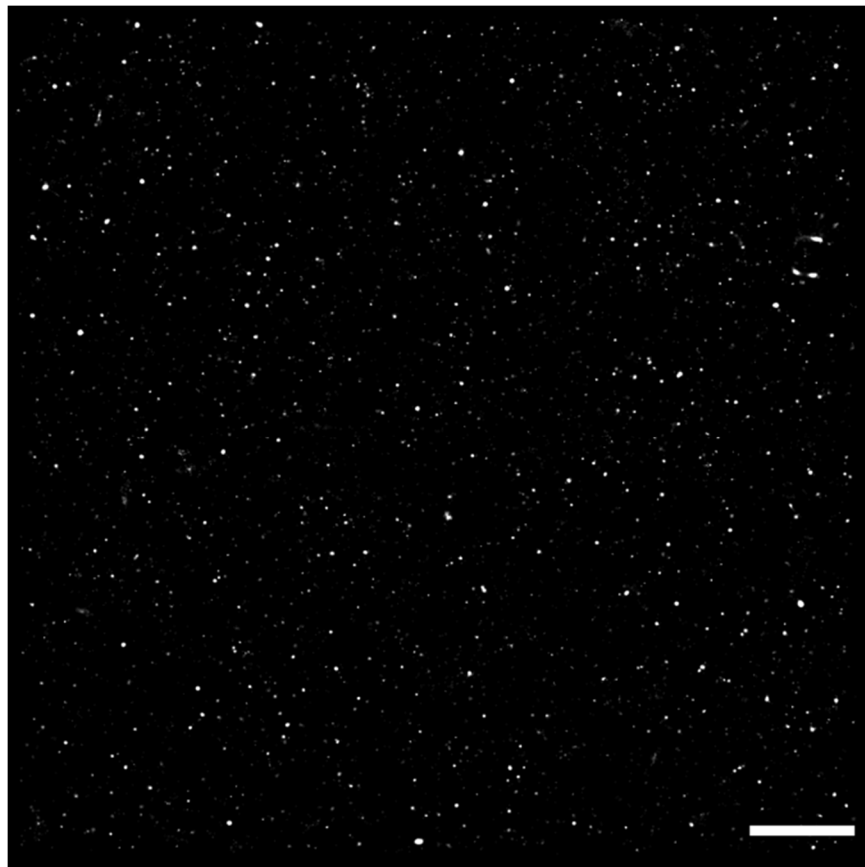


Figure S11: Super-resolution image of an undyed PMMA film (40 nm thick, 350 kg/mol). No elongated features appear. Small, round features appear, which are a result of fluorescent contaminants in the system. These unwanted fluorescent species have little effect on the resulting super-resolution images in dyed samples. Scale bar is 2 μm .

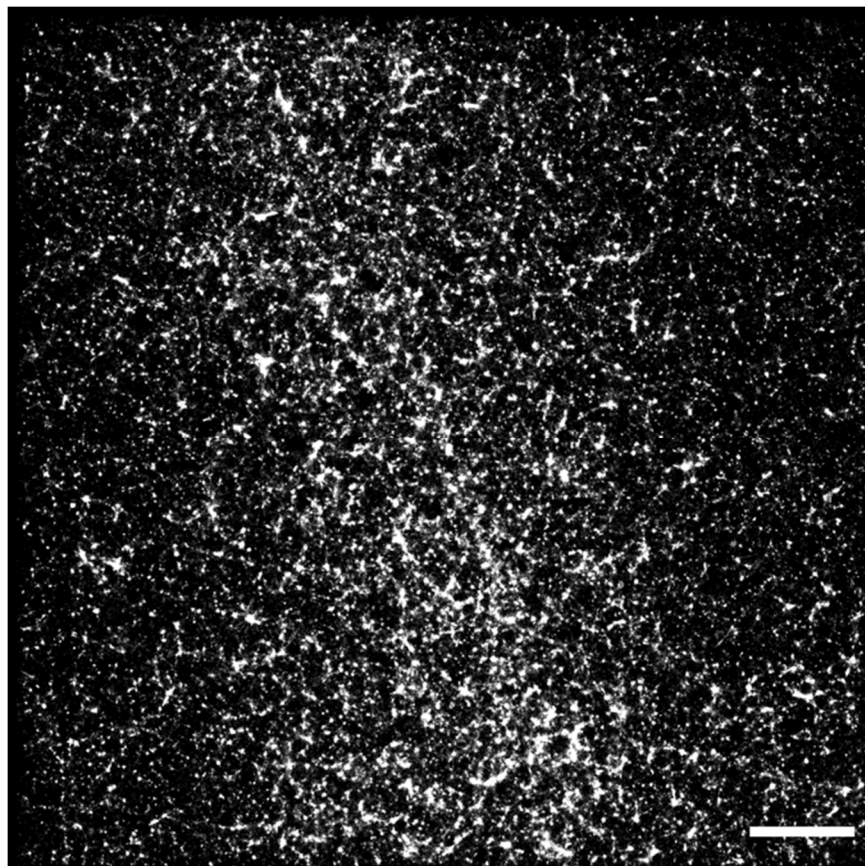


Figure S12: Super-resolution image of PMMA film (40 nm thick, 350 kg/mol) with free dye molecules introduced into the system. The concentration of the dye was chosen to approximately match the dye concentration within samples containing dyed bottlebrush polymer, which was approximately 0.00075% by mass. The free dye causes high fluorescent background that appears throughout the sample. Defined linear features do not appear within this image. Scale bar is 2 μm .

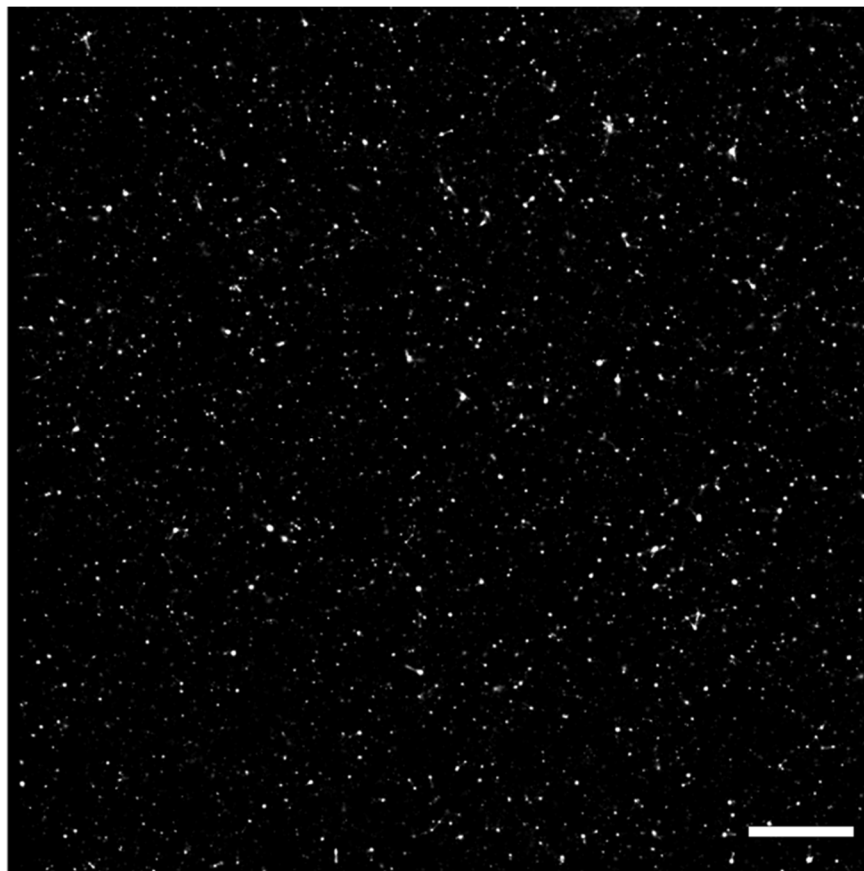


Figure S13: Super-resolution image of PMMA film (40 nm thick, 350 kg/mol) with a dilute amount of 4,800 g/mol dyed linear PMMA (0.01:1 dyed to undyed polymer). While there are numerous small, blob-like features from the dyed species, no defined elongated features appear. Scale bar is 2 μm .

9. Details for simulating super-resolution bottlebrush images

Worm-like chains (WLCs) were simulated to provide test data to support our bottlebrush analysis methods. These simulated chains were comprised of a series of unit vectors, and the angles between vectors was restricted to reflect WLC behavior. Angle values were obtained through inverse transform sampling, with the cumulative distribution derived from the bending energy for WLCs. The persistence lengths (l_p) and contour lengths (L_0) of generated chains were easily varied by inputting different values into the simulation. To simulate the noise of super-resolution images, the points along the chain were offset by a random distance from a normal distribution with standard deviation given by σ . Simulated localizations were plotted in ImageJ to produce pseudo-super-resolution images, which were then tested against our analysis tool. A total of 1,000 chains were generated and converted into super-resolution images for each condition, and the values for l_p and L_0 were extracted from skeletonization analysis and compared to the inputted values. The results for the fitted l_p are summarized in Figure 7, and the results for L_0 are summarized in Figure S14.

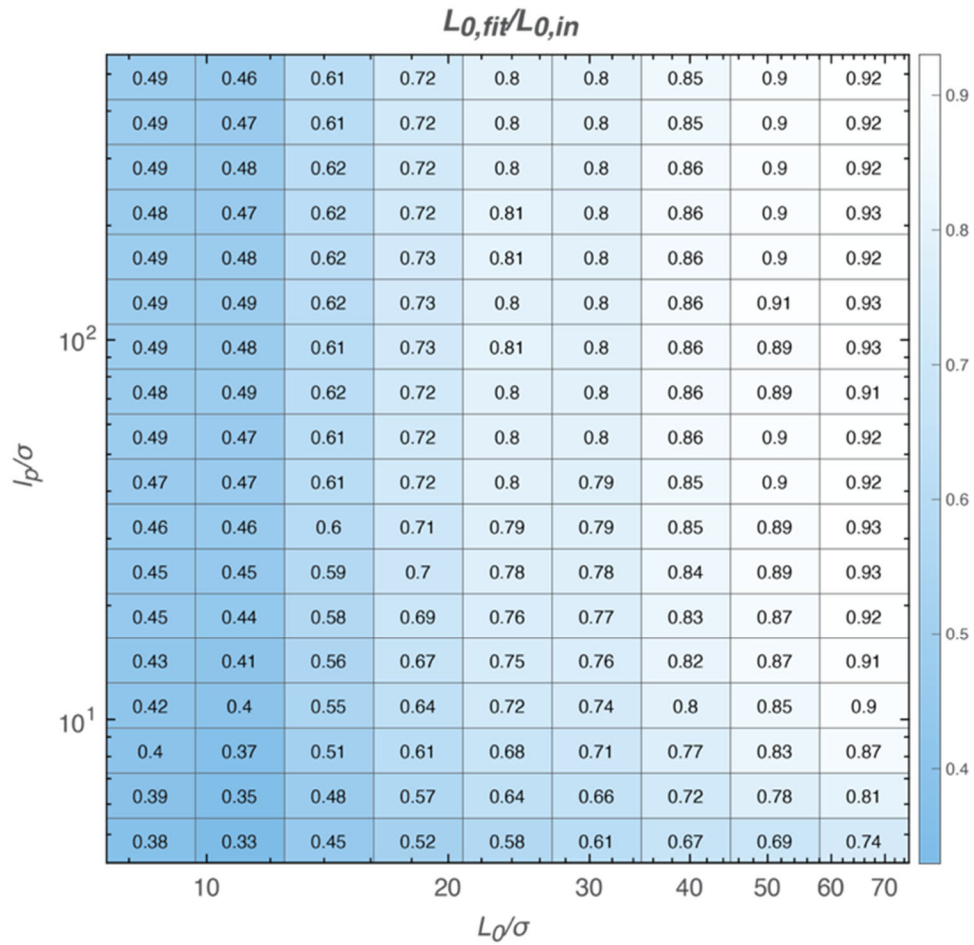


Figure S14: Simulation fits for contour length L_0 . The fitted L_0 is underestimated for all cases because during skeletonization, the traced curve does not go from end to end of the feature. This underestimation is particularly drastic for shorter features, where noise is comparable to the length of the feature, and for more flexible chains, where the bending is not precisely traced through skeletonization.

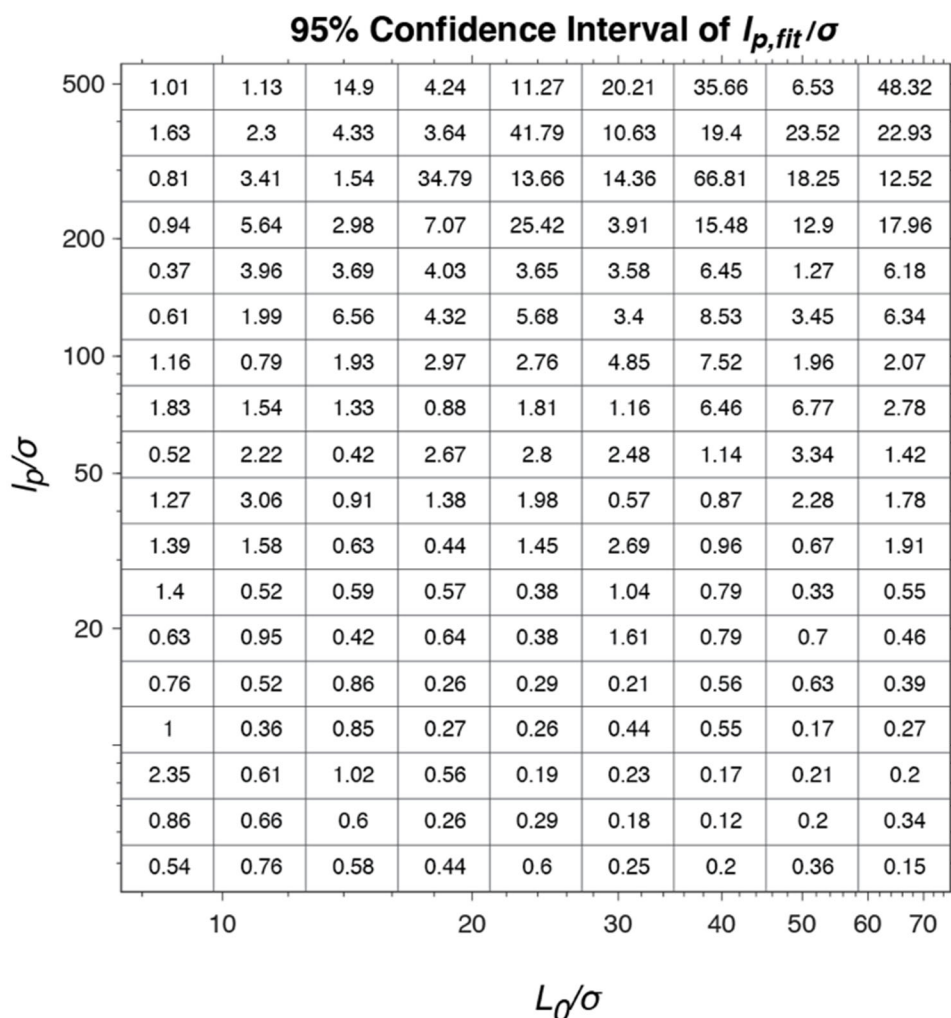


Figure S15: 95% confidence intervals of $l_{p,fit}/\sigma$ as determined using our skeletonization analysis tools. These confidence intervals are based on the variation in l_p as determined using our tools on ten sets of one hundred chain ensembles.

10. Comment on bottlebrush width and side chain length

The intrinsic error associated with super-resolution microscopy arises from the uncertainty of localizing a fluorescent event. This uncertainty is on the order of ten nanometers, which is above the expected side chain lengths used in this study which span lengths on the order of single nanometers. The widths of bottlebrushes are not expected to be affected by side chain length. To test this, we performed the same analysis to determine localization uncertainty, σ , and compared this value across different side chain length conditions. We have found that σ varies insignificantly between different conditions, and there is no trend that arises between side chain length and the width of the bottlebrush features.

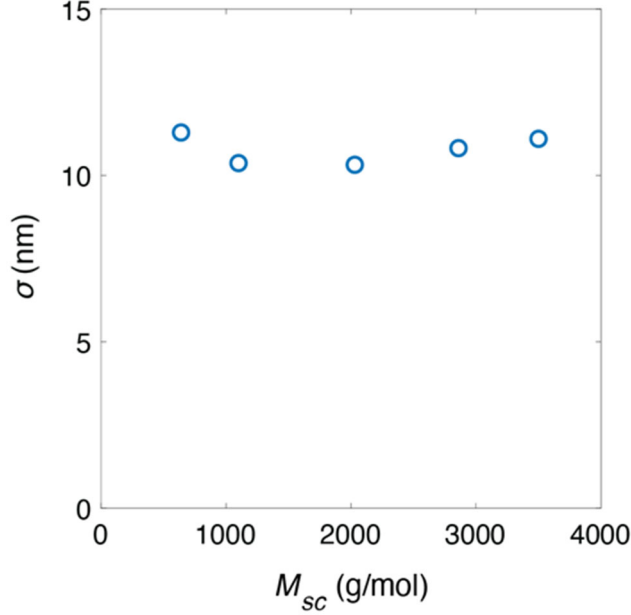


Figure S16: Plot of localization uncertainty σ vs. M_{sc} . Values of σ fall within a narrow range, and no trend between σ and M_{sc} is observed.

11. Monte Carlo simulation exploring effect of confinement on persistence length

To investigate whether confinement affects the persistence length of a wormlike chain with a given bending potential, we performed Monte Carlo simulations. Polymers were represented as freely-jointed chains with $N = 31$ beads connected by bonds of fixed length $ds = 10$ nm, leading to a total contour length of $L_0 = 300$ nm. A bending potential,

$$U = k_B T \frac{l_p}{ds} (1 - \cos \theta), \quad (1)$$

was applied to all adjacent bonds, where θ was the angle between bonds (Fig. S17). $l_p = 250$ nm was used for all of our conditions. Chains were first generated randomly in 3D according to Boltzmann factors using Equation (1). During each Monte Carlo step, each bead was attempted to be moved to a randomly selected position that preserves the bond lengths, and this new position was accepted according to the Metropolis criterion. The end beads were moved to new positions according to Equation (1). Wormlike statistics were verified by calculating the tangent-tangent correlation function $C(s)$, which decayed exponentially with a constant of $l_p = 250$ nm for the initialized chains and after every time step, as expected. 500 chains were simulated.

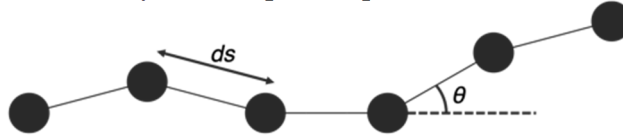


Figure S17: Polymers are represented as freely-jointed chains with a bending potential.

To simulate confinement in a thin film, for beads that attempted to move to any position outside of the region $0 < z < z_{max}$, these attempts were automatically accepted if they moved towards the film. This acts as an essentially infinitely steep potential that moves all of the beads into the film. After all of the beads were confined to the film (within 1000 MC steps for randomly initialized chains in 3D), we monitored the end-to-end correlation function, which decayed to zero after

2×10^6 MC steps for all conditions (Fig. S18). This removes any potential equilibration effects from the confinement process. The simulation then continued for another 3×10^6 MC steps, during which we stored bead and bond positions every 1000 MC steps to calculate $C(s)$. We simulated 500 chains for each of 3 film thicknesses of $z_{max} = 20, 40,$ and 60 nm.

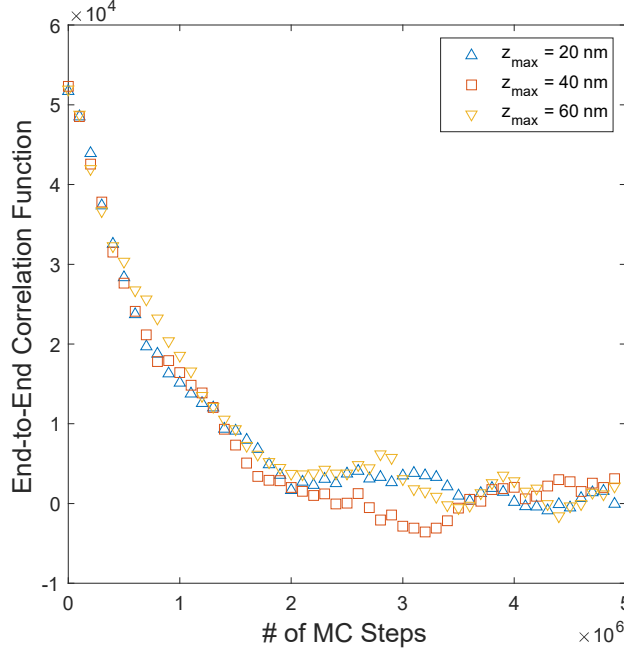


Figure S18: The end-to-end correlation function of the polymers confined to $z_{max} = 20, 40,$ and 60 nm.

To closely match the 2D imaging experiments described in the main body, we calculated the 2D $C(s)$ by simply ignoring the z positions of each bead. We confirmed an exponential decay according to the equation,

$$C(s) = e^{-s/2l_p}, \quad (2)$$

which is also shown as Equation (1) in the main body. The persistence lengths systematically underestimated the true $l_p = 250$ nm value (Fig. S19A), because the contour length in 2D is less than the full $L_0 = 300$ nm in 3D, as fluctuations in the small but finite z direction are not captured in the 2D projections. This effectively “shrinks” the s -axis in the $C(s)$ function, leading to a faster exponential decay and thus a smaller apparent l_p . As expected, this effect is diminished for smaller film thicknesses, as the apparent l_p values were 217, 228, and 238 nm for film thicknesses of $z_{max} = 60, 40,$ and 20 nm. Of note, the 40 nm thickness used in the experiments results in an underestimation of only 9% relative to the true value of $l_p = 250$ nm, and thus this effect is ignored in the main body.

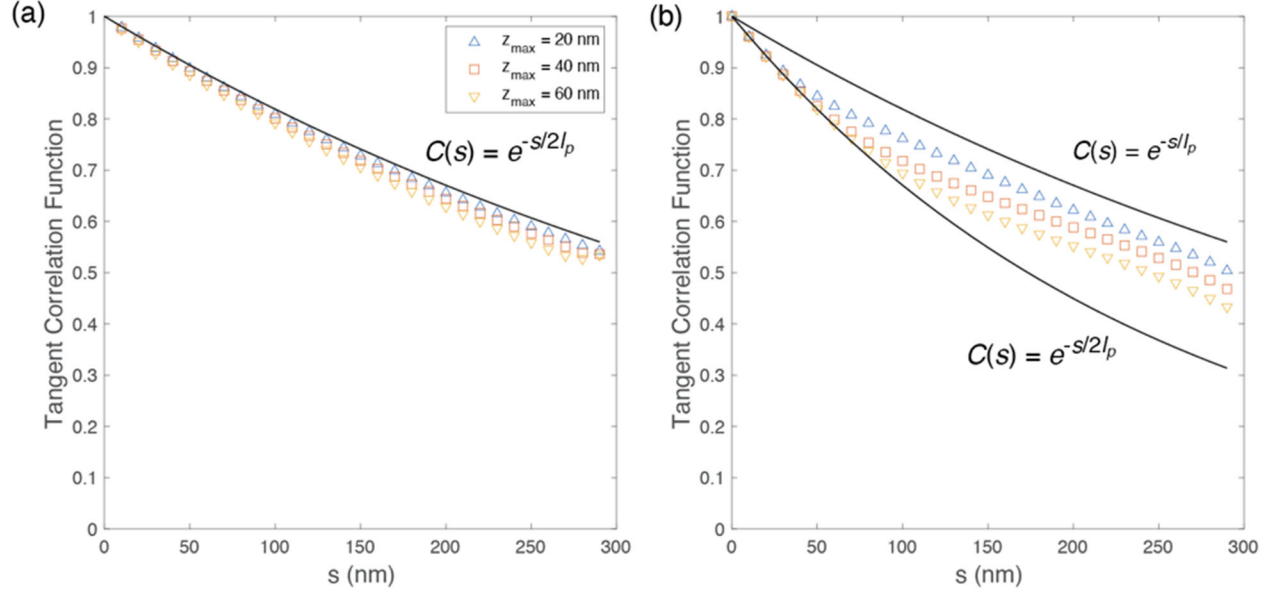


Figure S19: A) The 2D tangent-tangent correlation function of the polymers confined to $z_{max} = 20, 40,$ and 60 nm. Equation (2) is shown with $l_p = 250$ nm to guide the eye. **B)** The 3D tangent-tangent correlation function. The legend is identical to (A), and Equations (2) and (3) are shown.

We also calculated $C(s)$ in 3D for each of the three film thicknesses (Fig. S19B). All of the correlation functions show clear evidence of a double exponential decay. For small s , $C(s)$ decreases according to the equation,

$$C(s) = e^{-s/l_p}, \quad (3)$$

which simply describes wormlike statistics in 3D. However, when s increases beyond a certain critical value the chains begin to feel the presence of the confinement, and $C(s)$ transitions to the 2D confined behavior described by Equation (2). This critical value occurs at smaller s for smaller z_{max} , hence the higher values of $C(s)$ for smaller film thicknesses.

Overall, these simulation results confirm that thin film confinement has minimal effect on the statistics of a wormlike chain. This can be directly applied to the bottlebrush polymers explored in the experiments. Because the bending potential in the experiments is dominated by steric effects between the side chains, and because size of the side chains is on the order of single nanometers and much smaller than the 40 nm film thickness, we expect that the bending potentials in our thin film experiments should directly translate to those in a bulk 3D material. As our simulations show that polymers of the same bending potential will result in identical wormlike statistics either confined in thin films or not, this means that l_p measured in our 2D imaging experiments should be an accurate measure of l_p in 3D.